Electronic Supplementary Information

Polarized, color-selective and semi-transparent organic photodiode of aligned merocyanine H-aggregates

Tim Schembri, [ab] Leonhard Kolb, [ab] Matthias Stolte [ab] and Frank Würthner *[ab]

Table of Contents:

[a] *Universität Würzburg, Institut für Organische Chemie, Am Hubland, Würzburg 97074, Germany.*
[b] *Universität Würzburg, Center for Nanosystems Chemistry (CNC), Theodor-Boveri-Weg, Würzburg 97074, Germany*
** Corresponding author E-mail: wuerthner@uni-wuerzburg.de*

Experimental and Calculation Procedures

Preparation of PEDOT:PSS thin films:

PEDOT:PSS (= poly(3,4-ethylenedioxythiophene):polystyrene sulfonate) films were prepared by spincoating a colloidal suspension of PEDOT:PSS in water with a solid content of 1.3-1.7 % (PEDOT:PSS 1:6 *w*:*w*, *Heraeus*). The suspension was ultrasonicated at room temperature for 30 min and filtered through a 0.45 µm hydrophilic PVDF syringe filter (*Kinesis group*) prior to spincoating (*POLOS*™, *SPS-Europe spincoater*) in a lamellar flowbox (*WIBO barrier® BAKVO 180/91*, *Weisstechnik*). The substrates were covered with the suspension and spincoated at 2500 rpm with 4000 rpm s^{-1} acceleration for 30 s using a static dispense method. The substrates were then thermally annealed on a precision heating stage (*Harry Gestigkeit GmbH*) for 30 min at 240 °C. This annealing procedure was optimized according to literature.[S1]

As substrate, 2.5 × 2.5 cm^2 glass or glass/ITO (= indium tin oxide, *Soluxx GmbH*, sheet resistance of 15 Ω $□^{-1}$, 16 mm diameter circular ITO pattern) was used. The substrates were cleaned by ultrasonication (*VWR Ultrasonic Cleaner*) in acetone for 15 min and then mechanically brushed using a *Kärcher WB 120* disk-brush for 5 min at 60 rpm with light contact pressure in an aqueous detergent solution (*Mucasol*™, 1 vol% in deionized water). They were successively ultrasonicated in a new detergent solution (15 min), deionized water (3 × 10 min) and isopropanol (15 min). This was followed up by a 30 min ultraviolet/ozone treatment (*UVO-Cleaner®*, *Jetlight Company Inc.*).

Solution shearing:

Solution shearing was performed under ambient conditions using a custom shearing device (see Figure S1 for a schematic drawing and a photograph). The device includes a mechanically driven Si/SiO_2 wafer as a coating blade, which is brought into contact with the substrate at an angle of 20° and dragged across it with a defined speed of 0.083 mm s^{-1} using a linear actuator (*motor mike*, *Oriel Instruments*). The substrate surface is kept at a constant temperature of 70 °C or 85 °C during coating using a *Harry Gestigkeit GmbH* precision heating stage for the deposition of layers on PEDOT:PSS-coated glass substrates or on Si/SiO_2 wafers for transistors, respectively. For PEDOT:PSS-coated glass substrates a 0.5 mg mL^{-1} and for Si/SiO_2 wafers for transistors a 1.0 mg mL^{-1} solution of **1(Pyrl)**, which was synthesized according to its literature known procedure,[S2] in chlorobenzene (anhydrous grade, *Sigma Aldrich*) was used. Prior to shearing, the Si/SiO_2 wafers were cleaned by rinsing them with toluene, acetone, and isopropanol successively, which was followed up by a 30 min ultraviolet/ozone treatment (*UVO-Cleaner®*, *Jetlight Company Inc.*).

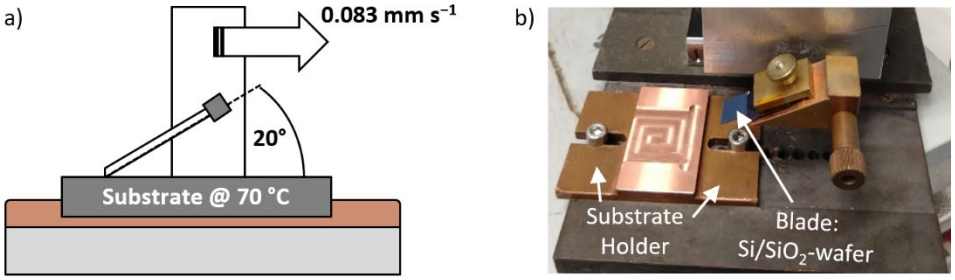

Figure S1. Schematic drawing (a) and photograph (b) of the custom-built device used for solution shearing.

Polarized and isotropic absorption spectroscopy:

UV-Vis-NIR absorption spectra were recorded using a *PerkinElmer Lambda 950* spectrophotometer equipped with a 150 mm integration sphere. The initial light beam was depolarized using the spectrometer's internal common beam depolarizer and optionally polarized using an integrated mechanically-controlled polarizer. Spectroscopic data was collected and averaged across the measurement of three independent samples.

Atomic force microscopy (AFM):

AFM images were recorded with a *Solver Next NT-MDT* microscope in semi-contact mode. A *SCOUT 350 RAI* (*Nu Nano Ltd*) silicon cantilever with a spring constant of 42 N m^{-1} and resonance frequency of 350 kHz was used.

Spincoating:

Spincoating was performed according to optimized literature parameters for OPD application[S3] from 1.5 mg mL^{-1} solutions of **1(Pyrl)** in chloroform (anhydrous grade, *Sigma Aldrich*). A solution volume of 120 µL was applied using a static dispense method at 3000 rpm s^{-1} and 3000 rpm for 30 s. Subsequentially, the thin films were annealed at 130 °C for 5 min on a *Harry Gestigkeit GmbH* precision heating stage. As opposed to literature, this process was performed under ambient instead of inert conditions to be directly comparable to the layers deposited by shearing.

Device fabrication:

For device fabrication of OTFTs and OPDs, the (PEDOT:PSS-)merocyanine-coated substrates were transferred to an *OPTIvap-XL* (*CreaPhys GmbH*) thermal evaporation system equipped with 6 MHz sensing crystals (*umicore*). All interlayer and active layer materials were evaporated at a pressure of $< 2 \times 10^{-6}$ mbar using a shadow mask at evaporation rates of 0.1, 0.2, 0.2, 0.3, and 0.1 Å s^{-1} for bathocuproine (BCP, 99.99 %, trace metal basis, *Sigma Aldrich*), fullerene $\mathbf{C_{60}}$ (2x sublimed, 99.9 %, *CreaPhys GmbH*), **NDI1** (as synthesized and purified according to literature[S4]), 1,4,5,8-naphthalenetetracarboxylic dianhydride (NTCDA, 1x sublimed, *Sigma Aldrich*), and 8-quinolinolato lithium (Liq, 1x sublimed, > 99 %, *Ossila*), respectively. The substrate holder was rotated at 10 rpm during evaporation to ensure more homogeneous layer deposition. Top electrode materials

Au (99.99 %, *umicore*) for OTFTs and Al (99.99 %, *MaTeck*) for OPDs were evaporated at rates of 0.1 to 0.3 and 0.1 to 3.0 Å s^{-1}, respectively, at a pressure of < 5 × 10^{-6} mbar using a shadow mask resulting in either OTFTs with 200 × 200 μm^2 contacts and 25 µm channel length or OPDs with 7.1 mm^2 active device area, respectively.

Transistor characterization:

Prior to measurement, individual OTFTs were isolated from each other by removing the organic semiconductor layer around the device with the needle of a micromanipulator. Transfer characteristics were recorded from +10 V to −50 V with 400 mV increments using an *Agilent 4055C* semiconductor parameter analyzer and a *Cascade EPS150* probe station under inert conditions (*M.Braun Inertgas Systeme GmbH*, UNIlab Pro, $c(O_2)$ < 1 ppm, $c(H_2O)$ < 1 ppm).

External quantum efficiency (*EQE*) and responsivity (*R*):

EQE measurements were performed at 0 V sample bias under inert conditions using a custom sample holder, a 300 W Xe ozone-free lamp (*6258*, *Oriel OPS-A500* Power Supply, *Newport*) as light source and an *Oriel 70710* (Gain = 10^5) pre-amplifier with a lock-in amplifier (*70104*, *Merlin*) for signal detection. Monochromic light was generated using an *Oriel Cornerstone™* (*260 ¼ m*, *74125*) monochromator with a chopping frequency of 180 Hz and the measurement referenced to a calibrated Si detector (*70356_70316NS*, Gain = 105). From the measured *EQE*, the responsivity *R* was calculated according to:

$$R = EQE \times \lambda \times e \times h^{-1} \times c^{-1},$$

where λ represents the wavelength, *e* the elementary charge, *h* the Planck constant, and *c* the speed of light in vacuum. For polarized *EQE* measurements, a triacetate dichroic film polarizer (*LPVISE2X2*, *Thorlabs*, see Figure S11 for spectral properties of the polarizer) was placed in contact with the bottom side of the OPD glass substrate. A schematic depiction of the measurement setup is given in Figure S12.

Current-density-voltage (*J-V*) characteristics:

J-V characteristics with AM1.5G illumination were measured under inert conditions (*M.Braun Inertgas Systeme GmbH*, UNIlab Pro, $c(O_2)$ < 1 ppm, $c(H_2O)$ < 1 ppm) using a parameter analyzer (*Botest Systems GmbH*) and a solar simulator (*Oriel Sol3ATM Class AAA*, *Newport®*) as a 1000 W m^{-2} AM1.5G light source. The lamp intensity was calibrated using a reference monocrystalline Si solar cell (*ISE CalLab*, KG-Filter). For blue-light *J-V* measurements, a 470 nm LED (*M470L5*, *Thorlabs*) was used, with its intensity set to 4.3 mW cm^{-2}. A comparison of lamp emission spectra with active layer absorption spectra is given in Figure S7. Devices were kept at 21 °C during measurements.

For linear dynamic range (*LDR*) measurements, neutral density filters (*NEK01S* filter kit, *Thorlabs*) with optical densities ranging from 0.1 to 4.0 were used. For polarized *J-V* measurements a Glan-Taylor prism

polarizer was used, which was manually rotated in steps of 10°. A schematic depiction of the measurement setup is given in Figure S12.

Cut-off frequency ($f_{-3\,dB}$) measurement:

For frequency response measurements of OPDs, the devices were illuminated by a 490 nm LED (*LED490L*, *Thorlabs*) within the custom *EQE* setup. The LED was pulsed with the built-in arbitrary function generator of a 100 MHz oscilloscope (*MDO32*, 2.5 GS s^{-1}, *Tektronix*) using a periodic square-wave function and signal readout occurred using the same oscilloscope with a parallel 50 Ω resistor (*FT500*, *Thorlabs*). For measurements up to 25 kHz a 100 kHz (*EF502*, *Thorlabs*) and above 25 kHz a 500 kHz (*EF506*, *Thorlabs*) electrical lowpass filter was used.

Noise current (I_{noise}) measurement:

Noise current I_{noise} was measured using a *Signal Recovery* Lock-in amplifier (*7265*, *AMETEK Scientific Instruments*) with the OPD shielded from all external light during measurement. The collected noise data at 180 Hz (corresponding to the chopping frequency during *EQE* measurements) was then used to calculate the specific detectivity D^* according to:

$$D^* = R \times A^{0.5} \times B^{0.5} \times {I_{noise}}^{-1},$$

where A is the device area (7.1 mm^2) and B the detection bandwidth (1 Hz).

Amsterdam Density Functional (ADF) calculations:

ADF was used to calculate the effective hole transfer integral (t_h) between all 12 nearest neighbors of **1(Pyrl)** taken from its crystal structure (CCDC deposition number: 1496525) for an estimation of the theoretical limit of the electrical dichroic ratio (DR_{el}). Therefor the ADF program[S5,S6] with the PW91 functional[S7] and a TZP basis set[S8] within the unique fragment approach[S9] was used. The t_h was then calculated according to reference [S10].

Literature Overview of Anisotropic Materials

Table S1. Overview of anisotropic polarization-sensitive (active layer) materials from literature including their different dichroic ratios: DR_{opt} – ratio of maximum to minimum absorption; DR_{el} – ratio of maximum to minimum mobility in transistors; DR_R – ratio of maximum to minimum photoresponse.

Material	Aligning method	DR_{opt}	DR_{el}	DR_R	Notes	Ref.
Small organic molecule: **1(Pyrl)**	Solution shearing + anisotropic single crystals / thin films	54	6.4	11	Narrowband, polarized and fully semi-transparent photodiode around 480 nm with a *FWHM* of 14 nm	This work
Small organic molecule: 2,6-diphenyl anthracene	Anisotropic single crystals	4	-	1.9	-	S11
Small organic molecule: perylene derivative	Mechanical rubbing	4-6	-	1.6	Article denotes that spectral overlap of donor and acceptor reduce DR_R compared to DR_{opt}	S12
Small organic molecule: squaraine	Solution shearing + anisotropic single crystals / thin films	6	21 *	-	Polarized transistor	S13
Small organic molecule: naphthalene diimide	Solution shearing + anisotropic single crystals / thin films	5 *	3 *	-	Polarized transistor	S14
Small organic molecule: naphthalene diimide and perylene bisimide derivatives	Off-center spincoating + anisotropic single crystals / thin films	1.4; 3.7	-	-	Polarized memory device	S15
2D material: $PdSe_2$	Anisotropic single crystals / thin films	3-4 *	-	54-112	Broadband photodiode	S16
2D material: bP/MoS_2	Anisotropic single crystals / thin films	-	-	22 **	IR-selective photodiode	S17
2D material: GeAs/InSe	Anisotropic single crystals / thin films	-	-	18	-	S18
2D material: bP/InSe	Anisotropic single crystals / thin films	-	-	11	-	S19
2D material: bP/WSe_2	Anisotropic single crystals / thin films	-	-	6 *	IR-selective photodiode	S20
2D material: $PdSe_2$	Anisotropic single crystals / thin films	5 *	-	4.5	Polarized transistor	S21
2D material: GeS_2	Anisotropic single crystals / thin films	1.3 *	-	2.1	UV-selective phototransistor	S22
2D material: $ReSe_2$	Anisotropic single crystals / thin films	-	-	-	Polarized transistor	S23
Nanowire: InP	Anisotropic single crystal	-	-	49	Narrowband around 870 nm with a *FWHM* of 75 nm *	S24
Nanowire: Bi_2Se_2S	Anisotropic single crystal	2 *	-	1.2 → 375	Universal polarization-sensitive amplification system to boost polarized photodiodes	S25
Nanowire: SbI_3/Sb_2O_3	Anisotropic single crystal	1.5-2.5	-	2-3	-	S26
Polymer: PBnDT-FTAZ:P(NDI2OD-T2)	Mechanical rubbing	9	-	9 *	Broadband, polarized photodiode	S27
Polymer: PNDI-TFx	In-situ molecular assembly	7 *	-	3.7	BHJ assembled by a floating film transfer method	S28
Polymer: PBnDT-FTAZ:P(NDI2OD-T2)	Mechanical stretching	1.8	-	1.4	Stretchable, broadband, and polarized photodiode	S29
Polymer: P3HT	Mechanical rubbing	25	8 *	-	Polarized transistor	S30
Polymer: C8-BTBT:PS	Off-center spincoating	2-3 *	-	-	Polarized transistor	S31
Perovskite: see reference	Anisotropic single crystals	-	-	35	-	S32
Perovskite: see reference	Anisotropic single crystals	-	-	25	-	S33
Perovskite: $(iso\text{-}BA)_2PbI_4$	Anisotropic single crystals	2 *	-	> 1	Narrowband photodiode around 560 nm with a *FWHM* of 27 nm using charge-collection narrowing	S34

*: Estimated from corresponding experimental data (absorption or Raman data, mobility plots, photoresponse spectra, etc.) in the referenced publication.
**: As estimated in reference S16.

Baseline correction for proper determination of the optical dichroic ratio:

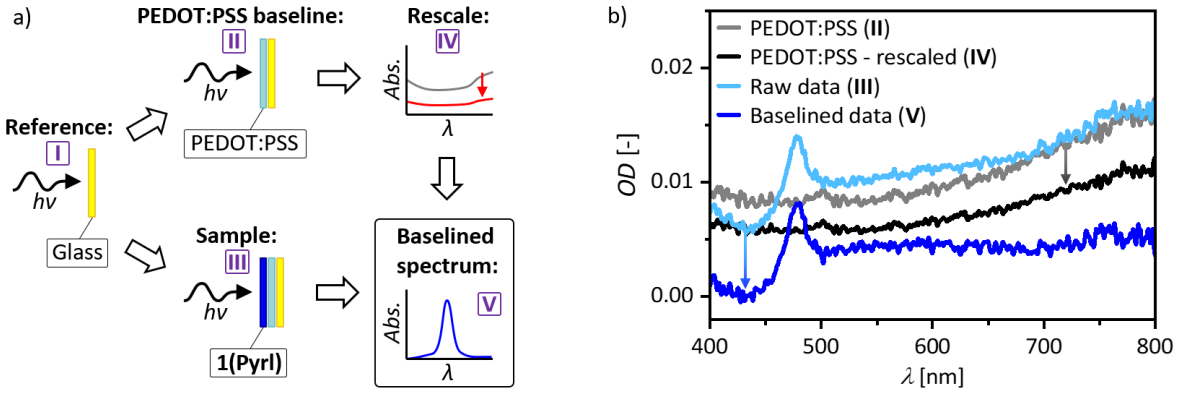

Figure S2. a) Schematic depiction of the workflow required for baseline correction of sheared **1(Pyrl)** layers on glass/PEDOT:PSS substrates. This involves the following steps, which all use linearly polarized light: **I** – recording a reference spectrum using an uncoated glass substrate; **II** – measuring the absorption of PEDOT:PSS, which is later used as the baseline; **III** – measuring the sample absorbance (this data now still includes parasitic absorption of PEDOT:PSS); **IV** – rescaling the PEDOT:PSS spectrum to match the sample spectrum (rescaling is only required if e. g., the PEDOT:PSS absorption differs due to deviations during the spincoating process); **V** – baselining the spectrum by subtracting the rescaled PEDOT:PSS absorption generated in step **IV** from the raw data generated in step **III**. b) An exemplary case of baseline correction of the absorbance of a sheared **1(Pyrl)** sample on a glass/PEDOT:PSS substrate at 0° polarization (parallel to the shearing direction); the black and blue arrows indicate the rescaling of PEDOT:PSS and baselining of the raw data as explained in steps **IV** and **V** in scheme a), respectively.

Polarization-dependency of sheared vs. spincoated films:

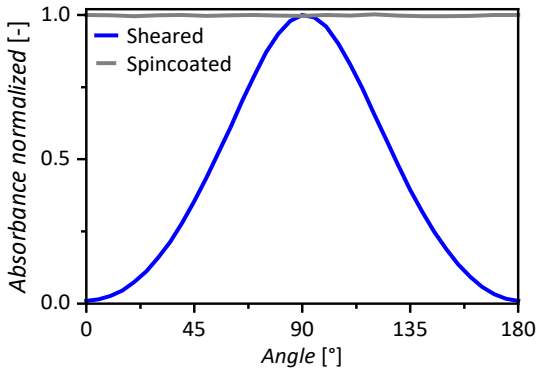

Figure S3. Polarization-dependent normalized absorbance at 478 nm of sheared (blue) and spincoated (grey) layers of **1(Pyrl)** on glass/PEDOT:PSS substrates. It is apparent, that the sheared layer shows sinusoidal dependency and the spincoated layer no dependency on the angle of light polarization.

Anisotropic vs. isotropic UV-Vis absorption spectroscopy:

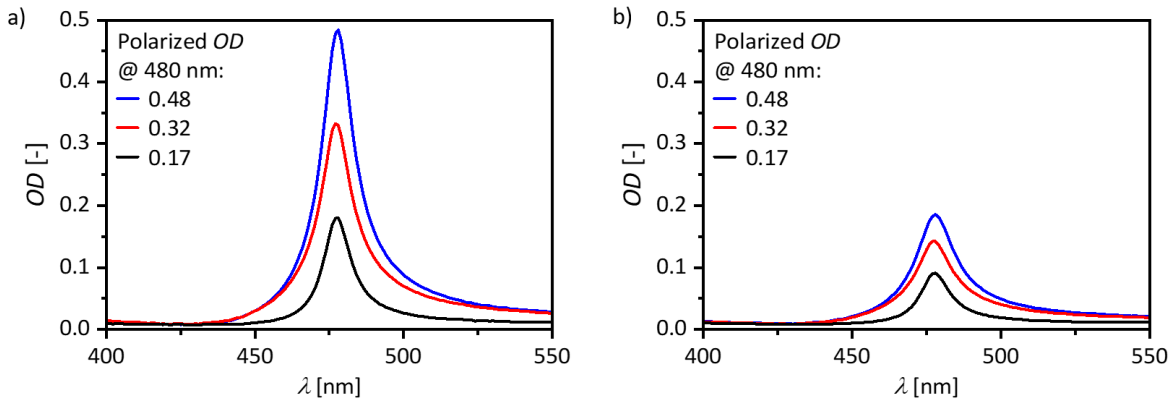

Figure S4. UV-Vis absorption spectra of sheared **1(Pyrl)** films on PEDOT:PSS with three different optical densities at the absorption maximum (0.48 – blue, 0.32 – red, 0.17 – black) measured under linearly (a) and isotropically polarized light (b) with respect to the shearing direction. The *OD* at 478 nm drops to about 0.19 (40 %), 0.14 (44 %) and 0.09 (53 %), respectively, when using isotropically polarized light instead of linearly polarized light for the same sample.

Atomic force microscopy (AFM) of sheared vs. spincoated layers:

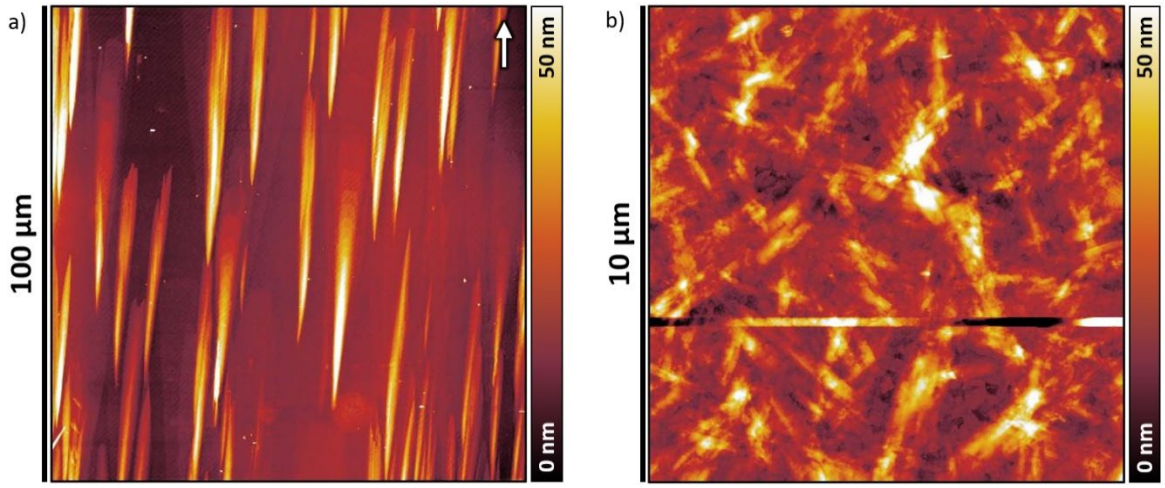

Figure S5. AFM images of sheared (a) and spincoated (b) layers of **1(Pyrl)** with identical optical density of isotropically polarized absorption / thickness; the white arrow in a) shows the respective shearing direction; the needle-like crystallites in a) show an extension over several tens of micrometers with unidirectional orientation, whereas the needle-like crystallites in b) show an isotropic orientation with a spatial extension reduced by one order of magnitude.

Organic Thin-Film Transistors

Organic thin-film transistor (OTFT) architecture:

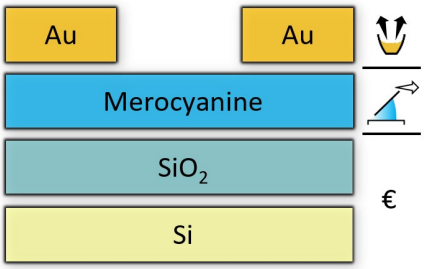

Figure S6. Schematic depiction of the bottom-gate, top-contact OTFT architecture used for the determination of the charge-transport electric dichroic ratio DR_{el}; the Si/SiO_2 substrate is commercially available, the merocyanine layer is deposited by solution shearing and the Au electrodes are deposited by thermal evaporation.

Atomic force microscopy (AFM) of transistor channels:

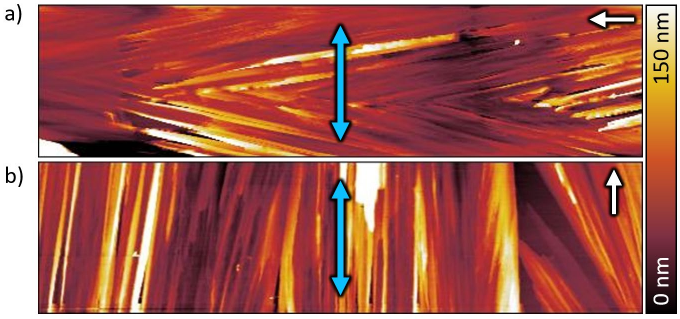

Figure S7. AFM images (100 µm × 25 µm) of the channels of OTFT devices perpendicular (a) and parallel (b) to the shearing direction; the double-sided blue arrows show the direction from drain to source electrodes of the OTFTs; the white arrows show the respective shearing directions.

Transistor figures of merit:

Table S2. Hole mobility μ_p, threshold voltage U_{th}, on-current I_{on} and the on/off-ratio I_{on} / I_{off} of OTFTs in an Si/SiO_2 (100 nm)/**1(Pyrl)**/Au (30 nm) bottom-gate, top-contact architecture with 200 µm channel width and 25 µm channel length measured perpendicular and parallel to the shearing direction. The data for both directions was averaged over 7 substrates with 5 devices per substrate (= 35 OTFTs in total). **1(Pyrl)** layers were sheared using the following parameters: c = 1 mg mL^{-1} in chlorobenzene, substrate temperature = 85 °C, shearing speed = 0.083 mm s^{-1}, shearing blade angle = 20°.

Direction	μ_p [$cm^2\ V^{-1}\ s^{-1}$]	U_{th} [V]	I_{on} [A]	I_{on} / I_{off} [-]
Perpendicular	$(2.1 \pm 1.3) \times 10^{-4}$	-10 ± 2	10^{-8}	10^3
Parallel	$(1.3 \pm 0.5) \times 10^{-3}$	-8 ± 1	10^{-7}	10^4

Theoretical Calculations

Amsterdam Density Functional (ADF) charge-transfer calculations:

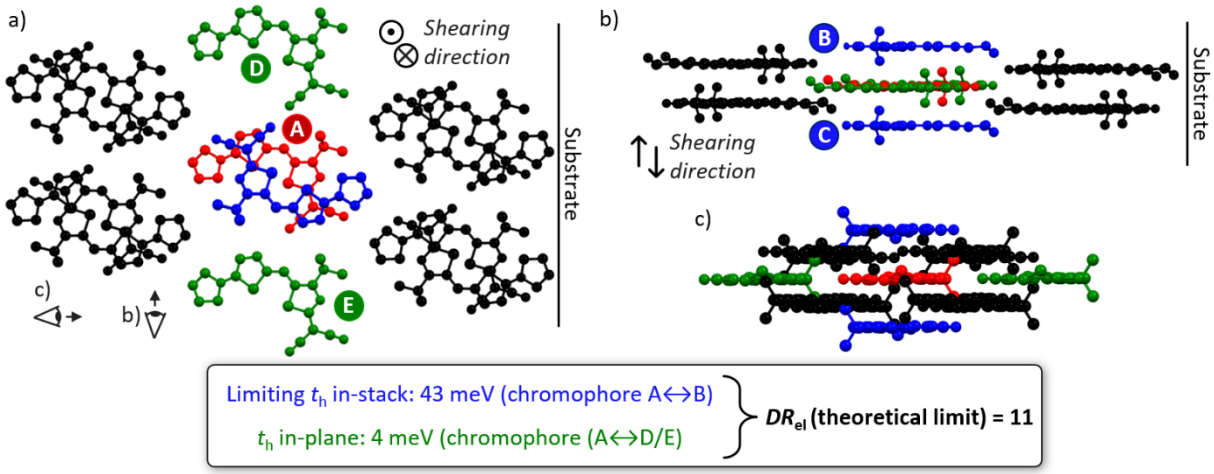

Figure S8. a-c) Depiction of all twelve nearest neighbors relative to chromophore A of **1(Pyrl)** in its crystal structure used for ADF charge-transfer calculations including the resulting theoretical electrical dichroic ratio of 11 as limited by the calculated effective hole-transfer integrals (t_h). In panel a) the viewpoints onto the chromophores used for panels b) and c) are shown. Calculated transfer integrals from A to out-of-plane chromophores shown in black were negligible (< 1 meV).

Organic Photodiodes

Light source and acceptor/donor spectra:

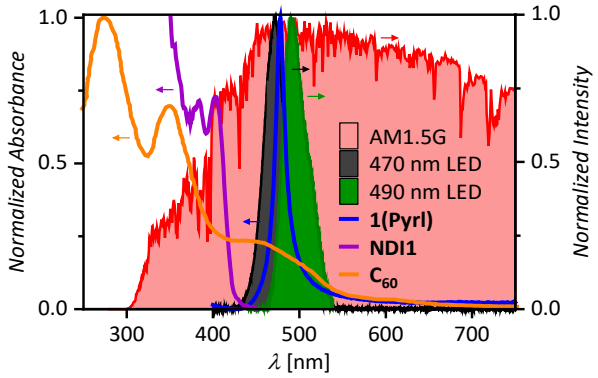

Figure S9. Normalized emission spectra of the different light sources (solid lines with filled graphs; AM1.5G solar simulator – red, *Thorlabs M470L5* LED – black, *Thorlabs LED490L* – green) used for OPD characterization shown in relation to the normalized absorbance (solid lines) of **1(Pyrl)** (blue), **NDI1** (violet), and **C_{60}** (orange).

Long-term device stability:

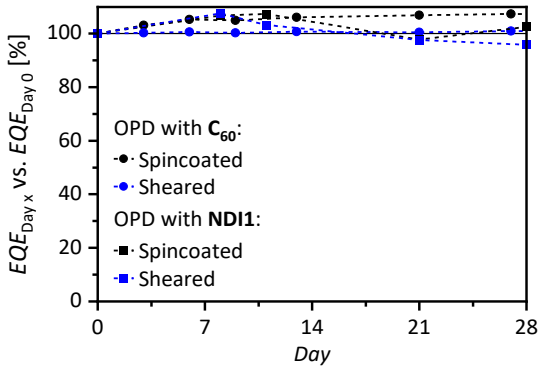

Figure S10. Long-term *EQE* measurement results showing the long-term *EQE* divided by the initial *EQE* ($EQE_{Day\ x}$ vs. $EQE_{Day\ 1}$) of OPDs with **C_{60}** (circle) or **NDI**1 (squares) as acceptor, both as spincoated (black) and sheared (blue) devices stored under inert glovebox conditions. The dashed lines serve as guide to the eye.

Organic photodiode figures of merit:

Table S3. Figures of merit of all OPD devices.
Glossary: J_{sc} = short-circuit current density; *FF* = fill factor; V_{oc} = open-circuit voltage; R_{max} = responsivity at maximum around 480 nm; $FWHM_R$ = full-width-at-half-maximum of the H-aggregate band around 480 nm; DR_R = photoresponse dichroic ratio; *AVT* = average visible transmittance; I_{noise} = noise density at 180 Hz; D^*_{max} = specific detectivity at maximum around 480 nm; *LDR* = linear dynamic range; $f_{-3\,dB}$ = cut-off frequency.

OPD	J_{sc} [1] [mA cm^{-2}]	*FF* [1] [%]	V_{oc} [1] [V]	R_{max} [2] [mA W^{-1}]	$FWHM_R$ [2] [nm, cm^{-1}]	DR_R [2] [-]	*AVT* [%]	I_{noise} [10^{-12} A Hz$^{-0.5}$]	D^*_{max} [10^9 Jones]	*LDR* [3] [-, dB]	$f_{-3\,dB}$ [kHz]
Spincoated, **C$_{60}$**	−0.68	46	0.22	36	33, 1 370	-	-	6.3	1.5	10^3, 40	190
Sheared, **C$_{60}$**	−0.70	50	0.41	57	23, 980	6	88	3.6	4.2	10^2, 20	135
Spincoated, **NDI1**	−0.06	43	0.63	5	21, 950	-	-	2.5	0.5	10^3, 40	6
Sheared, **NDI1**	−0.07	34	0.67	7	23, 940	11	93	2.5	0.7	10^3, 40	10

[1]: Values obtained with AM1.5G illumination and averaged over 14-31 devices with standard deviations below 18 %.
[2]: Values averaged over three devices.
[3]: The *LDR* denoted marks the lower limit of the *LDR*, whereby the measurement was limited by our measurement setup.

Linear dynamic range (LDR):

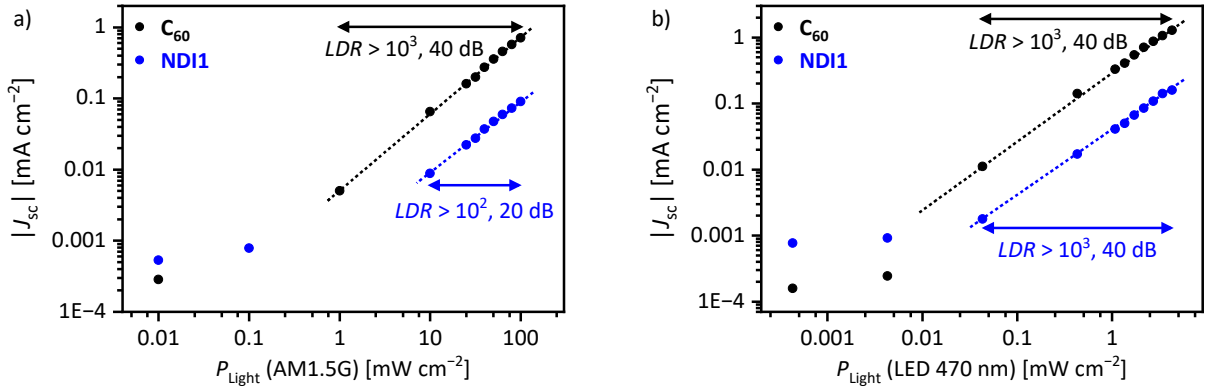

Figure S11. Linear dynamic range (*LDR*) measurements of the short-circuit current density (J_{sc}) plotted against the incident light power using either AM1.5G (a) or 470 nm LED illumination (b) of sheared OPDs with **C$_{60}$** (black) and **NDI1** (blue) as electron acceptor; the dashed lines and arrows serve as guides to the eye and highlight the *LDR*.

Frequency response measurements:

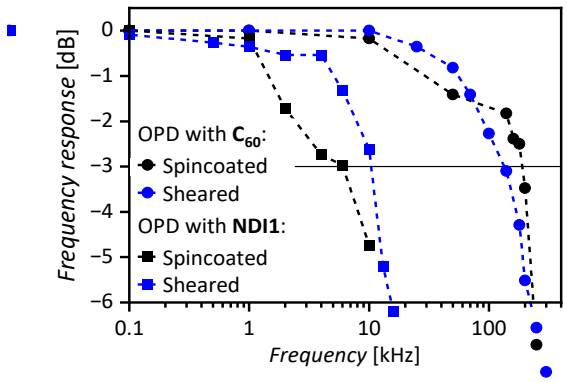

Figure S12. Frequency response measurements of OPDs with **C$_{60}$** (circle) or **NDI1** (squares) as acceptor, both as spincoated (black) and sheared (blue) devices, under 490 nm LED illumination. The dashed lines serve as guide to the eye. The horizontal line marks the −3 dB threshold.

Optical properties of dichroic film polarizer for EQE measurements:

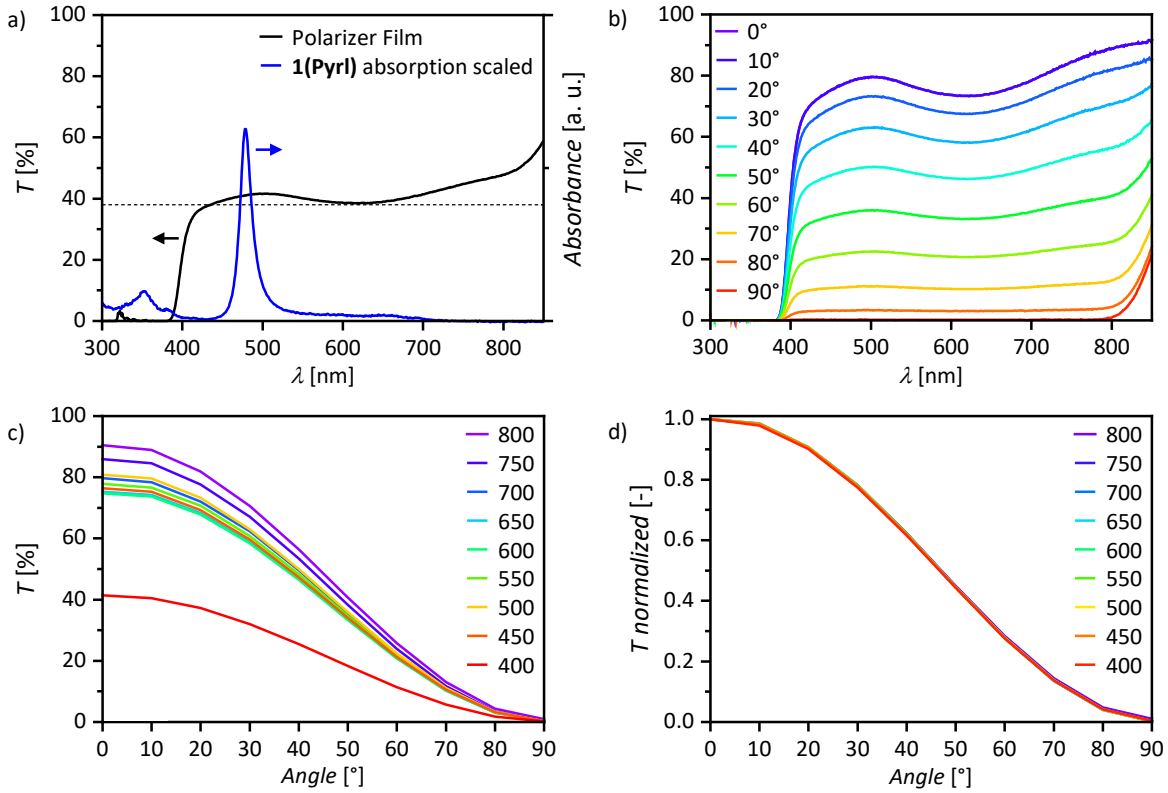

Figure S13. Transmission data of the triacetate dichroic film polarizer used for isotropic *EQE* measurements. a) Isotropic transmission (*T*) spectrum compared to the scaled absorbance of **1(Pyrl)**. b) Polarized/anisotropic transmission spectra in steps of 10° with the initial light polarized with the integrated Glan-Taylor polarizer of a *Lambda950* spectrometer. c) and d) show the transmission and normalized transmission, respectively, in dependence of the polarization at different wavelengths; in d) the sinusoidal behavior of the dichroic film polarizer across the entire visible light range is apparent.

Measurement setups for polarized *J-V* and *EQE* measurements:

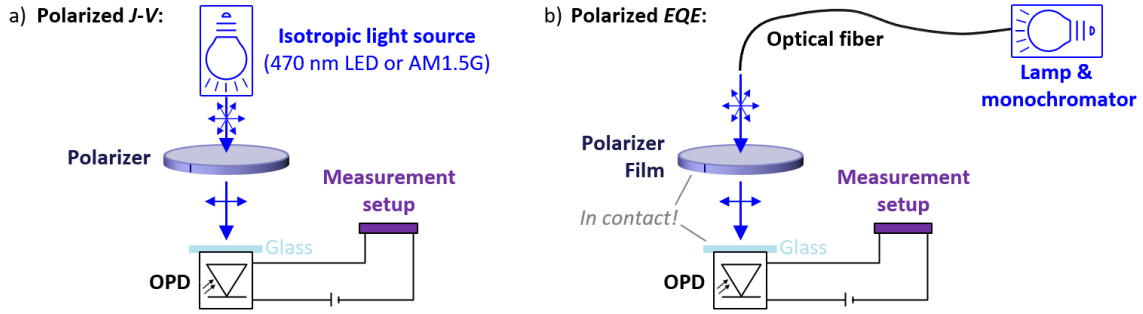

Figure S14. Schematic measurement setups for polarized OPD characterizations *via* polarized *J-V* (a) and polarized *EQE* (b) measurements.

Current-density-voltage (*J*-*V*) measurements:

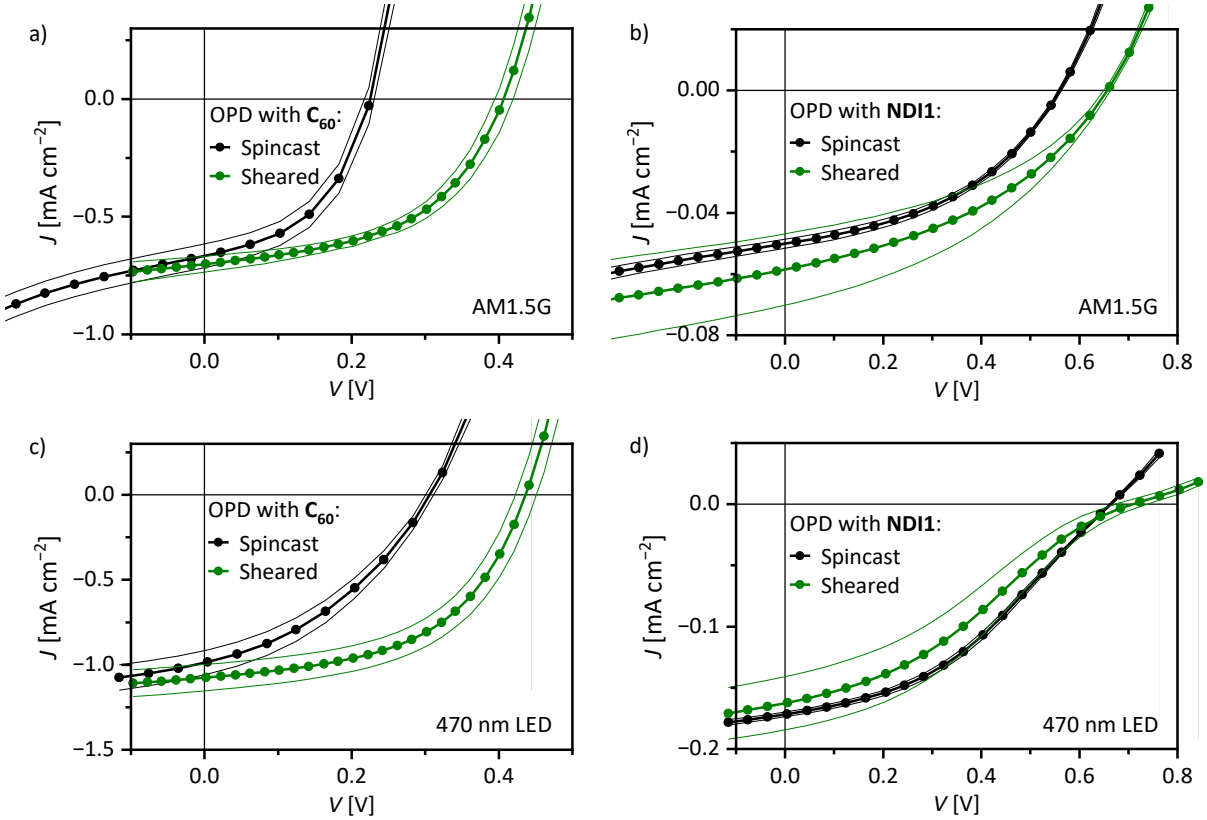

Figure S15. a) and b) show the current-density-voltage (*J*-*V*) graphs under AM1.5G illumination of OPDs with C_{60} or **NDI1** fabricated *via* spincoating (black) or shearing (green), respectively; the lines serve as guide to the eye; the shaded area marks the standard deviation average across ≥ 6 devices. c) and d) show the corresponding graphs under selective 470 nm LED illumination.

Supporting References

S1 B. Friedel, P. E. Keivanidis, T. J. K. Brenner, A. Abrusci, C. R. McNeill, R. H. Friend and N. C. Greenham, *Macromolecules*, 2009, **42**, 6741–6747.

S2 A. Liess, A. Lv, A. Arjona-Esteban, D. Bialas, A.-M. Krause, V. Stepanenko, M. Stolte and F. Würthner, *Nano Lett.*, 2017, **17**, 1719–1726.

S3 T. Schembri, J. H. Kim, A. Liess, V. Stepanenko, M. Stolte and F. Würthner, *Adv. Optical Mater.*, 2021, **9**, 2100213.

S4 D. Shukla, S. F. Nelson, D. C. Freeman, M. Rajeswaran, W. G. Ahearn, D. M. Meyer and J. T. Carey, *Chem. Mater.*, 2008, **20**, 7486–7491.

S5 G. Te Velde, F. M. Bickelhaupt, E. J. Baerends, C. Fonseca Guerra, S. J. A. van Gisbergen J. G. Snijders and T. Ziegler, *J. Comput. Chem.*, 2001, **22**, 931–967.

S6 ADF 2013, SCM, Theoretical Chemistry, Vrije Universiteit, Amsterdam, The Netherlands, http://www.scm.com.

S7 J. P. Perdew, K. Burke and Y. Wang, *Phys. Rev. B*, 1996, **54**, 16533–16539.

S8 P. L. Barbieri, P. A. Fantin and F. E. Jorge, *Mol. Phys.*, 2006, **104**, 2945–2954.

S9 K. Senthilkumar, F. C. Crozema, F. M. Bickelhaupt and L. D. A. Siebbeles, *J. Chem. Phys.* 2003, **119**, 9809–9817.

S10 S.-H. Wen, A. Li, J. Song, W.-Q. Deng, L.-K. Han and A. Goddard, *J. Phys. Chem. B*, 2009, **113**, 8813–8819.

S11 T. Wang, K. Zhao, P. Wang, W. Shen, H. Gao, Z. Qin, Y. Wang, C. Li, H. Deng, C. Hu, L. Jiang, H. Dong, Z. Wei, L. Li and W. Hu, *Adv. Mater.*, 2022, **34**, 2105665.

S12 H. Tanaka, T. Yasuda, K. Fujita and T. Tsutsui, *Jpn. J. Appl. Phys.*, 2005, **44**, 8676–8678.

S13 M. Gsänger, E. Kirchner, M. Stolte, C. Burschka, V. Stepanenko, J. Pflaum and F. Würthner, *J. Am. Chem. Soc.*, 2014, **136**, 2351–2362.

S14 M. Stolte, M. Gsänger, R. Hofmockel, S.-L. Suraru and F. Würthner, *Phys. Chem. Chem. Phys.*, 2012, **14**, 14181–14185.

S15 J. H. Kim, M. Stolte, F. Würthner, *ACS Nano*, 2022, **16**, 19523–19532.

S16 D. Wu, J. Guo, J. Du, C. Xia, L. Zeng, Y. Tian, Z. Shi, Y. Tian, X. J. Li, Y. H. Tsang and J. Jie, *ACS Nano*, 2019, **13**, 9907–9917.

S17 J. Bullock, M. Amani, J. Cho, Y.-Z. Chen, G. H. Ahn, V. Adinolfi, V. R. Shrestha, Y. Gao, K. B. Crozier, Y.-L. Chueh and A. Javey, *Nature Photon.*, 2018, **12**, 601–607.

S18 J. Xiong, Y. Sun, L. Wu, W. Wang, W. Gao, N. Huo and J. Li, *Adv. Optical Mater.*, 2021, **9**, 2101017.

S19 S. Zhao, J. Wu, K. Jin, H. Ding, T. Li, C. Wu, N. Pan and X. Wang, *Adv. Funct. Mater.*, 2018, **28**, 1802011.

S20 L. Ye, P. Wang, W. Luo, F. Gong, L. Liao, T. Liu, L. Tong, J. Zang, J. Xu and W. Hu, *Nano Energy*, 2017, **37**, 53–60.

S21 D. Wu, M. Xu, L. Zeng, Z. Shi, Y. Tian, X. J. Li, C.-X. Shan and J. Jie, *ACS Nano*, 2022, **16**, 5545–5555.

S22 Y. Yang, S.-C. Liu, X. Wang, Z. Li, Y. Zhang, G. Zhang, D.-J. Xue and J.-S. Hu, *Adv. Funct. Mater.*, 2019, **29**, 1900411.

S23 E. Zhang, P. Wang, Z. Li, H. Wang, C. Song, C. Huang, Z.-G. Chen, L. Yang, K. Zhang, S. Lu, W. Wang, S. Liu, H. Fang, X. Zhou, H. Yan, J. Zou, X. Wan, P. Zhou, W. Hu and F. Xiu, *ACS Nano*, 2016, **10**, 8067–8077.

S24 J. Wang, M. S. Gudiksen, X. Duan, Y. Cui and C. M. Lieber, *Science*, 2001, **293**, 1455–1457.

S25 W. Ran, Z. Ren, P. Wang, Y. Yan, K. Zhao, L. Li, Z. Li, L. Wang, J. Yang, Z. Wei, Z. Lou and G. Shen, *Nat. Commun.*, 2021, **12**, 6476.

S26 M. Xiao, H. Yang, W. Shen, C. Hu, K. Zhao, Q. Gao, L. Pan, L. Liu, C. Wang, G. Shen, H.-X. Deng, H. Wen and Z. Wei, *Small*, 2020, **16**, 1907172.

S27 A. Altaqui, P. Sen, H. Schrickx, J. Rech, J.-W. Lee, M. Escuti, W. You, B. J. Kim, R. Kolbas, B. T. O'Connor and M. Kudenov, *Sci. Adv.*, 2021, **7**, eabe3196.

S28 Z. Shao, F. Yu, G. Cen, T. Gu, X. Huang, Y. Wang, W. Cai, W. Mai, X. Xu, D. Qin, R. Yang, L. Hou, *Appl. Phys. Lett.*, 2023, **124**, 043301.

S29 P. Sen, R. Yang, J. J. Rech, Y. Feng, C. H. Y. Ho, J. Huang, F. So, R. J. Kline, W. You, M. W. Kudenov and B. T. O'Connor, *Adv. Optical Mater.*, 2019, **7**, 1801346.

S30 A. Hamidi-Sakr, L. Biniek, S. Fall and M. Brinkmann, *Adv. Funct. Mater.*, 2016, **26**, 408–420.

S31 Y. Yuan, G. Giri, A. L. Ayzner, A. P. Zoombelt, S. C. B. Mannsfeld, J. Chen, D. Nordlund, M. F. Toney, J. Huang and Z. Bao, *Nat. Commun.*, 2014, **5**, 3005.

S32 W. Zhang, M. Hong and J. Luo, *J. Am. Chem. Soc.*, 2021, **143**, 16758–16767.

S33 R. Li, Z. Wang, T. Zhu, H. Ye, J. Wu, X. Liu and J. Luo, *Angew. Chem. Int. Ed.*, 2023, **62**, e202308445.

S34 L. Li, L. Jin, Y. Zhou, J. Li, J. Ma, S. Wang, W. Li and D. Li, *Adv. Optical. Mater.*, 2019, **7**, 1900988.